

Modeling and design of an X-band rf photoinjector

R. A. Marsh,* F. Albert, S. G. Anderson, G. Beer, T. S. Chu, R. R. Cross, G. A. Deis, C. A. Ebberts,
D. J. Gibson, T. L. Houck, F. V. Hartemann, and C. P. J. Barty
Lawrence Livermore National Laboratory, Livermore, California 94550, USA

A. Candel, E. N. Jongewaard, Z. Li, C. Limborg-Deprey, A. E. Vlieks, F. Wang, J. W. Wang,
F. Zhou, C. Adolphsen, and T. O. Raubenheimer
SLAC National Accelerator Laboratory, Menlo Park, California 94025, USA
(Received 28 March 2012; published 15 October 2012)

A design for an X-band rf photoinjector that was developed jointly by SLAC National Accelerator Laboratory (SLAC) and Lawrence Livermore National Laboratory (LLNL) is presented. The photoinjector is based around a 5.59 cell rf gun that has state-of-the-art features including: elliptical contoured irises; improved mode separation; an optimized initial half cell length; a racetrack input coupler; and coupling that balances pulsed heating with cavity fill time. Radio-frequency and beam dynamics modeling have been done using a combination of codes including PARMELA, HFSS, IMPACT-T, ASTRA, and the ACE3P suite of codes developed at SLAC. The impact of lower gradient operation, magnet misalignment, solenoid multipole errors, beam offset, mode beating, wakefields, and beam line symmetry have been analyzed and are described. Fabrication and testing plans at both LLNL and SLAC are discussed.

DOI: [10.1103/PhysRevSTAB.15.102001](https://doi.org/10.1103/PhysRevSTAB.15.102001)

PACS numbers: 07.77.Ka, 29.25.Bx, 29.27.-a, 41.75.Ht

I. INTRODUCTION

The development of rf photoinjector technology has enabled free electron lasers and other fourth generation light sources, such as the Linac Coherent Light Source (LCLS) at SLAC National Accelerator Laboratory (SLAC). At Lawrence Livermore National Laboratory (LLNL) a novel gamma-ray light source is being developed and built taking advantage of inverse Compton scattering to extract energy from high brightness electron bunches to boost laser photons to MeV energies. At SLAC advanced compact X-band (11.424 GHz) photoinjector R&D is being done to investigate the possibility of generating short enough high brightness electron bunches that at least one stage of bunch compression may become unnecessary, as well as to enable an all X-band free-electron laser by establishing a proven electron beam source.

Nuclear resonance fluorescence (NRF) is a process in which a nucleus, excited by gamma rays, reradiates high-energy, very narrow bandwidth photons. Because NRF energy levels depend on the exact nuclear structure of the emitter, NRF spectra are isotope specific. Monoenergetic gamma-ray (MEGa-ray) sources using Compton scattering and the detection of NRF resonances have applications in homeland security, nuclear waste assay, medical imaging, and stockpile surveillance. Currently, Compton scattering is

the only process capable of producing a narrow bandwidth radiation (below 1% $\Delta\omega/\omega$) at gamma-ray energies by using state-of-the-art accelerator and laser technologies. In Compton scattering sources, a short laser pulse and a relativistic electron beam collide to yield tunable, monochromatic, polarized gamma-ray photons. Building on prior work on narrowband gamma-ray light sources at LLNL [1–8], the LLNL Nuclear Photonics Facility (NPF) will be equipped with a tunable MEGA-ray source using an all X-band linac including an X-band rf photoinjector. The advantages of operating at X band and further detail on the linac design are available in [9].

This paper describes an rf photoinjector which will be tested at the X-band test area (XTA) at SLAC, at an X-band test station at LLNL, and will serve as the injector for the X-band very energetic light for the observation and characterization of isotopic resonances and the assay and precision tomography of objects with radiation (VELOCIRAPTOR) linac, designed to drive the precision, compact, MEGA-ray source at the NPF [9]. The XTA will be built parallel to the Next Linear Collider Test Accelerator (NLCTA) beam line, and use a single 105 cm traveling wave accelerator structure to produce bunches of ~ 100 MeV so that they can be accurately measured using a combination of diagnostics including: emittance measurement via quad scan technique [10], profile measurements on optical transition radiation and yttrium aluminum garnet screens, charge measurement via Faraday cup, and slice emittance using an X-band transverse deflecting structure. The X-band test station at LLNL will use a single 53 cm traveling wave accelerator structure to produce up to 50 MeV electron bunches, and will serve as a platform for future X-band development at LLNL.

*marsh19@llnl.gov

Published by the American Physical Society under the terms of the [Creative Commons Attribution 3.0 License](https://creativecommons.org/licenses/by/3.0/). Further distribution of this work must maintain attribution to the author(s) and the published article's title, journal citation, and DOI.

An X-band rf gun has been designed and operated at SLAC as reported in [11–13]. This Mark 0 structure achieved peak electric fields of 200 MV/m on the cathode surface. In collaboration, LLNL and SLAC have designed and extensively modeled a new Mark 1 rf gun building on the experience with the Mark 0. The X-band rf guns are both 6 cell design, supporting 6 eigenmodes including the 11.424 GHz π mode that will be used for acceleration. The Mark 1 rf gun improves on the Mark 0 design to produce a higher quality electron bunch with less chance of rf breakdown. A computer-aided design (CAD) rendering of the Mark 1 rf gun is shown in Fig. 1. The major design modifications include: a geometry change from circular cross-section irises to elliptical contoured; an iris thickness adjustment to improve mode separation; a longer initial half cell; a racetrack coupler; and input rf coupling to balance pulsed heating with cavity fill time. A combination of design codes were used including: PARMELA [14,15], HFSS [16], IMPACT-T [17], ASTRA [18], and the ACE3P suite of codes developed at SLAC [19,20].

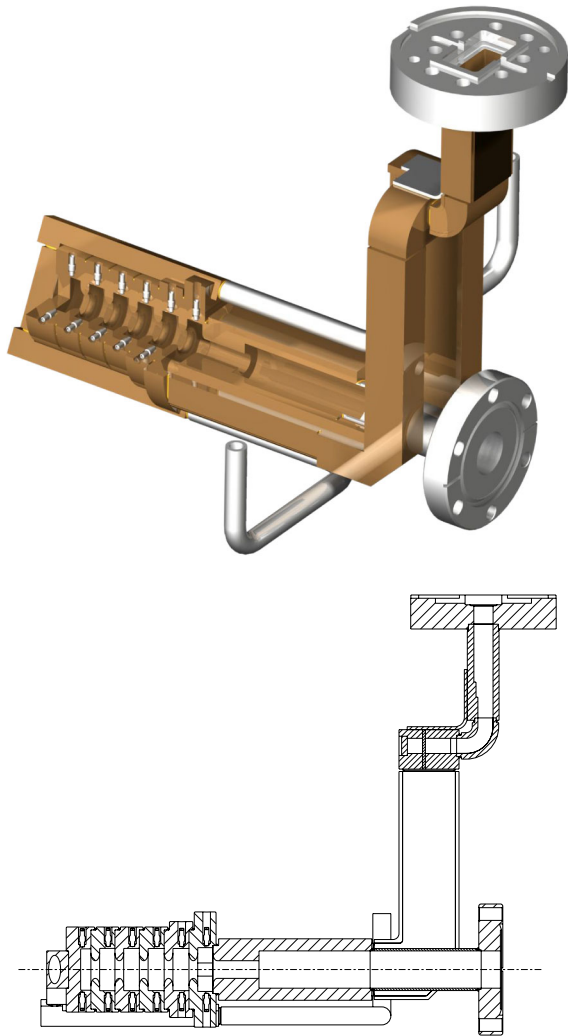


FIG. 1. CAD rendering and schematic of the Mark 1 X-band rf gun.

TABLE I. Mark 1 rf gun parameters.

Frequency	11.424 GHz
Unloaded quality factor	7055
First cell length	0.59 cell
Coupler type	Dual feed racetrack
Iris shape	Elliptical, 1.8 major/minor
Mode separation	25 MHz
Cathode material	Oxygen-free high conductivity
Cathode peak field	200 MV/m
Final kinetic energy	7 MeV

A Mark 2 X-band rf gun is currently being designed to include a removable photocathode, as well as incorporating design changes found necessary by operational experience with Mark 0 and Mark 1 guns. Modifications that are being considered for the Mark 2 include: removable photocathode geometry including the ability to use higher quantum efficiency materials, rf pickups for a direct measurement of gun field magnitude and phase, a more symmetric cooling channel, and a redesigned solenoid with lower field asymmetry.

In the following sections, more detail is given on the design and trade-off considerations for the Mark 1 LLNL/SLAC gun, solenoid, and subsequent accelerator sections. The Mark 1 parameters are summarized in Table I. The photoinjector that will be used in the LLNL NPF will need to be as robust as possible to minimize downtime and maximize the number of photons delivered to the greatest number of experiments. The number of photons extracted via inverse Compton scattering scales with N_e/ϵ^2 [9]; the goal for this rf photoinjector is an rms emittance as far below 1 mm mrad as possible at 250 pC. These considerations drive improvements in the Mark 1 rf gun, and future generation designs.

II. RF DESIGN

The rf gun design process began in 2D with SUPERFISH runs providing field maps for PARMELA beam dynamics simulations. The 2D design allowed the cells to be rapidly tuned to achieve field flatness, mode frequency, before modeling the gun performance. 2D modeling was also used to determine elliptical iris profile, and to tune the first cell length. 3D modeling using HFSS and ACE3P was required to determine the final cell dimensions and to optimize the racetrack coupler. The final design requirement was to generate a 250 pC bunch with minimal transverse emittance, while lowering the peak surface electric field on the irises, improving the mode separation, balancing the longitudinal electric field from cell to cell, and achieving an optimized coupling with an rf-quadrupole-minimized racetrack coupler.

A. Initial 2D design

Beginning with the Mark 0 rf gun parameters, the code SUPERFISH was used to alter the cell geometry and iris

parameters. Measurement of the Mark 0 rf gun confirmed that the distance between the operating π mode and the nearest neighboring mode was <10 MHz as designed, and time domain modeling of the multiple eigenmodes simultaneously excited in the Mark 0 gun showed that the nearest mode would still have a significant excitation at the nominal fill time as a result. In order to generate as bright a beam as possible, the mode separation was increased to 25 MHz, at which point mode beating contributes a negligible emittance increase. The mode separation was increased to 25 MHz by increasing the iris radius to 4.6736 mm and thinning the iris slightly to a thickness of 4.6228 mm.

An important use of the fast running 2D codes is tuning cavity parameters for field flatness and correct frequency; the most critical dimension in this regard is the cavity radius for each of the 6 cells. The fast run time of SUPERFISH meant that the cells could be tuned beyond 4 significant figures to achieve a very flat field from cell to cell and a π mode at exactly 11.424 GHz. This 2D optimum provided a starting point for 3D optimization.

Although circularly shaped irises are typically used in rf guns and accelerators, the shape can be made elliptical, which can lower the peak surface electric field for the same axial electric field [21]. Though this change increases the surface area with a high field, it should lower the probability of rf breakdown. The optimal elliptical profile varies with iris geometry, and depends on the iris radius and thickness. The iris radius and thickness for the Mark 1 rf gun are determined by the goal of increased mode separation, as discussed in Sec. II A, allowing an optimization of ellipticity for an iris radius of 4.6736 mm and an iris thickness of 4.6228 mm. The ellipticity chosen in 2D simulation and confirmed in 3D simulation has a major to minor ratio of 1.8. With this ratio, the peak surface electric field is about 10% lower than that for a circularly shaped iris.

The length of the first half cell can have a strong impact on the final beam emittance. For any given cell length, there is a different optimal laser injection phase and emittance compensation solenoid field strength. By varying the cell length and retuning the entire design, the effect of cell length alone can be isolated, and a final cell length can be determined. The final emittance also depends on the laser pulse shape and other external constraints, such as the length over which the emittance is compensated. For this design study the distance from the photocathode to the entry

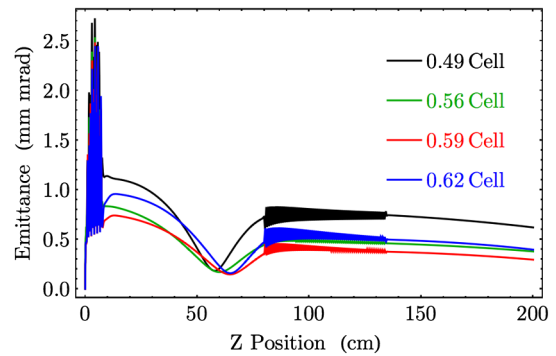


FIG. 2. Normalized emittance of a 250 pC bunch along the photoinjector for rf guns having different initial cell lengths.

point of the traveling wave accelerator section was fixed at 80 cm. The laser pulse profile was assumed to be a clipped Gaussian transversely, with a temporal shape corresponding to the stacking of 8 short pulses. Table II summarizes the photocathode drive-laser pulse parameters [22].

For this laser pulse, a parameter study was completed to find the optimal first cell length by changing the first cell length, flattening the field and adjusting the operating frequency, and then optimizing the injection phase and emittance compensation solenoid magnetic field strength. The design study assumed the operation of a T53 accelerator section located at a distance of 80 cm from the cathode position operating at an accelerating gradient of 75 MV/m. Results are shown in Fig. 2 for four designs, with a first cell length of 0.59 cell being optimal.

Either a single Gaussian laser pulse or two stacked Gaussian pulses will be used at the SLAC XTA, but the optimum cell length is still close to 0.59 so this length was adopted.

B. Circuit model

In order to analyze the rf gun response to realistic input pulses, a circuit model was developed using full 3D HFSS simulation results as a starting point, including: unloaded quality factor (Q_0) and coupling coefficient (β); the driver cell, middle cell, and end cell frequencies; the shunt impedance; the generator impedance; the input power level for a peak surface electric field of 200 MV/m on the cathode; and the generator frequency for the π mode (standing wave mode with 180° phase advance per cell). The elaborate circuit model was validated against HFSS and found to be in good agreement. This was done by exciting the π mode in both an HFSS driven simulation and a circuit model calculation and comparing the electric field magnitude and phase, as shown in Table III.

The circuit model was first used to compare its prediction of the rf gun energy gain to that predicted by the beam dynamics modeling code. In particular, the circuit model included the characteristic input rf pulse shape from a SLED-II pulse compressor, which is part of the X-band rf system at SLAC that will be used to power the

TABLE II. Photocathode drive-laser parameters.

Wavelength	263.25 nm
Energy	50 μ J
Transverse σ	0.55 mm
Transverse hard edge	0.46 mm
Temporal rise/fall	250 fs
Temporal FWHM	2 ps

TABLE III. Electric field phase (deg) comparison between HFSS and circuit model.

Cell	HFSS	Circuit
1 (driver)	0	0
2	176.84	176.80
3	5.50	5.72
4	-172.93	-172.4
5	8.00	8.50
5.5	-171.65	-170.50

photoinjector. Very little deviation was seen in comparison to IMPACT-T results for beam energy gain after the 5.59 cells of the rf gun.

The circuit model was next used to optimize β . The input coupling to the rf gun was chosen as a trade-off between keeping the required rf pulse length short (which decreases pulsed heating [23,24] and the likelihood of rf breakdown), reducing the required input power (which simplifies the requirements on the rf source and the rf feed system, including the rf gun window), and generating the bunch when the cavity fields are near steady state (which decreases the sensitivity to timing jitter and minimizes the effect of transient excitation of nearby modes).

For a baseline input power of 17.7 MW, the required cavity pulse length fill time is plotted as a function of β in Fig. 3. Also shown are curves for larger input powers (10%, 20%, and 30%), and the corresponding peak pulsed heating in the regular rf gun cells. The peak heating is about a factor of 2 larger at the waveguide opening in the coupler cell, and in general, one wants to keep the heating below 50°C to prevent heating related breakdown enhancement [25,26]. From these curves, one can see that increasing the input power by 10% shortens the fill time and lowers the pulsed heating considerably for a broad range of β .

Assuming the baseline 100% input power, a β of 1.7 was chosen, which results in an rf pulse length of about 200 ns. This length is ~ 3 times the field time constant of 65 ns so the fundamental mode fields reach $\geq 95\%$ of their steady

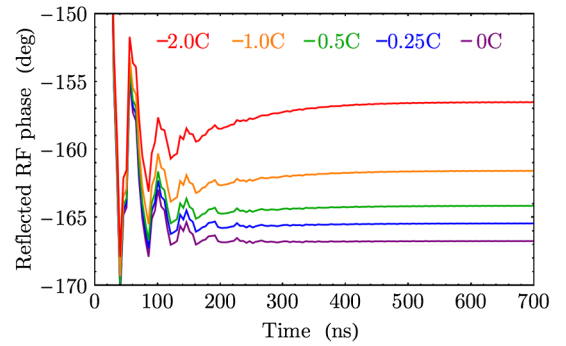


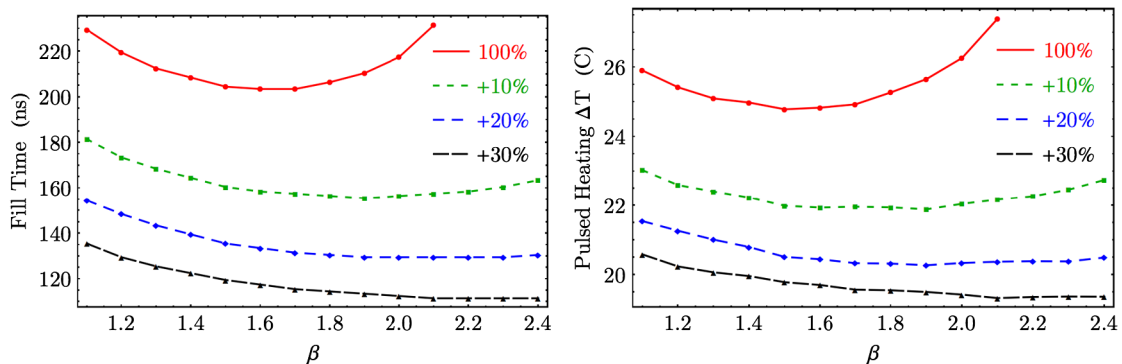
FIG. 4. Mark 1 X-band rf gun reflected power at the input port as a function of temperature change for a square input pulse.

state values. Using a square input rf pulse, the circuit model predicts that the field contribution from the neighboring modes is less than 2%. Tests will also be done at SLAC where the gun will be run at a 10% higher power with a 160 ns pulse. This lowers the pulsed heating significantly while still keeping the neighboring mode contribution less than 2%.

Finally, the circuit model was used to gauge the sensitivity of the reflected rf phase to the rf gun frequency, which depends on the operating temperature. A 1°C change in temperature detunes the rf gun by 190 kHz, which is $\sim 5\%$ of the cavity bandwidth. To keep the rf gun in tune, the temperature will be regulated to the 0.1°C level, and if necessary, the phase of the reflected rf will be regulated as well. Figure 4 shows circuit model simulations of how the phase varies with the rf gun temperature. These results show that a 0.5° X-band phase regulation near the nominal tune is equivalent to a 0.1°C temperature regulation. This agrees with that expected from a simple analytical treatment of the rf gun as a resonator.

C. Minimizing coupler asymmetry

The impact of the coupler fields on the beam dynamics was studied by analyzing the particle transverse momentum change after traversing the coupler fields [27,28]. In a

FIG. 3. Mark 1 X-band rf gun β for fill time to reach 200 MV/m cathode field, and the corresponding pulsed heating temperature rise. Curves are shown for the nominal input power (100%) and 10%, 20%, and 30% additional power.

periodic accelerator structure the lowest longitudinal Fourier component (β_z) of E_z can be expressed as

$$E_z(r, \theta, z, \beta_z) = \sum_{n=0}^{\infty} A_n J_n(\eta_r r) \cos(n\theta) e^{-i\beta_z z} + \sum_{n=0}^{\infty} B_n J_n(\eta_r r) \sin(n\theta) e^{-i\beta_z z}, \quad (1)$$

where $\eta_r^2 + \beta_z^2 = \omega^2/c^2$ and $J_n(\eta_r r)$ is the n th Bessel function. Assuming $\beta \approx 1$ and a straight trajectory, from the Panofsky-Wenzel [29] theorem, to first order in r , the transverse momentum ($p_{\perp}/m_0 c$) change is given by

$$\begin{aligned} \Delta(\gamma \vec{\beta}_{\perp}) &= \frac{ie}{m_0 c \omega} \left(\frac{\eta_r A_1}{2} \hat{x}_0 + \frac{\eta_r B_1}{2} \hat{y}_0 - \frac{\eta_r^2 A_0}{2} (x \hat{x}_0 + y \hat{y}_0) \right) \\ &+ \frac{ie}{m_0 c \omega} \left(\frac{\eta_r^2 A_2}{2} (x \hat{x}_0 - y \hat{y}_0) + \frac{\eta_r^2 B_2}{2} (y \hat{x}_0 + x \hat{y}_0) \right) \\ &= D_x \hat{x}_0 + D_y \hat{y}_0 + F(x \hat{x}_0 + y \hat{y}_0) + Q(x \hat{x}_0 - y \hat{y}_0) \\ &+ S(y \hat{x}_0 + x \hat{y}_0), \end{aligned} \quad (2)$$

where D_x and D_y are the rf dipole deflection in the x and y planes, F is the radial rf focusing, and Q and S are the quadrupole and skew quadrupole moments. The synchronous condition requires that $\eta_r^2 = \omega^2/c^2 - \beta_z^2 = -\omega^2/(v\gamma)^2$, where v is the particle velocity. Since $J_n(\eta_r r) \propto (\eta_r r)^n$ for small r and E_z is independent of γ , the E_z field expansion coefficients satisfy

$$A_0 = \text{constant} \quad A, B_1 \propto 1/\eta_r \propto \gamma \quad A_2, B_2 \propto 1/\eta_r^2 \propto \gamma^2. \quad (3)$$

As a result, the rf dipole D , and quadrupole Q and S factors are independent of γ while the radial focusing factor F is proportional to $1/\gamma^2$. The relative rms head-tail transverse momentum change ($\sigma_{\Delta p_{\perp}}$) results in a projected emittance growth, which can be approximated as follows in the x plane, for example, when $\beta_z \approx 1$ and the effect is small at a waist location:

$$\begin{aligned} \epsilon_{n,f} &= \sqrt{\epsilon_{n,i}^2 + \sigma_x^2 \left(\frac{\sigma_{\Delta p_x}}{m_0 c} \right)^2} \\ &\approx \epsilon_{n,i} \left(1 + \frac{\sigma_x^2 \sigma_{\Delta(\gamma \beta_x)}^2}{2 \epsilon_{n,i}^2} \right) \\ &\approx \epsilon_{n,i} \left(1 + \frac{1}{2} \left(\frac{\sigma_{\Delta(\gamma \beta_x)}/\gamma}{\sigma_{x'}} \right)^2 \right). \end{aligned} \quad (4)$$

Thus, the fractional emittance growth is roughly one half of the induced rms-squared angular spread divided by the incident beam angular spread squared. Having a small waist (low lattice beta) reduces the effect. Also, the induced angular spread depends on the phase of the higher multipole fields (being on the zero crossing produces the largest effect) and the growth is reduced with shorter bunches. Finally, the growth scales as $1/\gamma$ for the dipole kicks, $1/\gamma^2$ for the quadrupole kicks, and $1/\gamma^4$ for radial

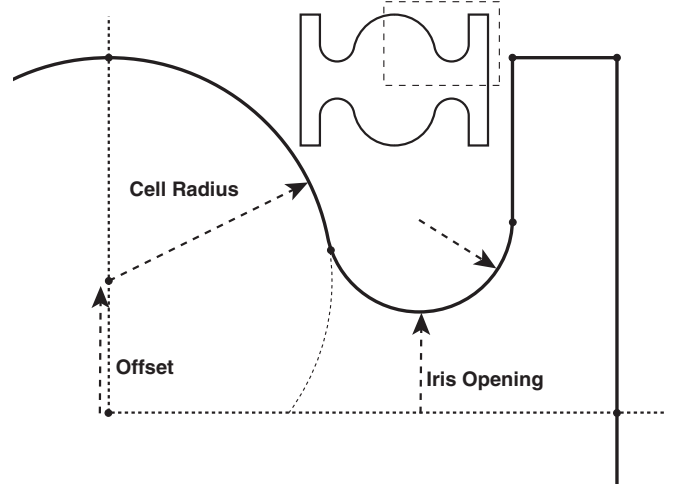


FIG. 5. Racetrack input coupler geometry; one quarter of the full cell is shown inset. The standard (round) coupler corresponds to an offset of zero.

kicks; thus, the emittance growth induced by the coupler multipole fields is more of a concern at lower energies.

This dipole head-tail effect can be eliminated via a symmetrized power feed. The quadrupole head-tail effect was minimized by using a racetrack shaped coupler geometry as shown in Fig. 5. A standard coupler has no offset, which results in a round cell profile; a nonzero offset results in a racetrack shaped coupler cell. The offset and cell radius were tuned for a given iris opening to achieve minimal $\Delta(\gamma \beta_{\perp})$. A significant improvement was achieved as illustrated in Fig. 6, which compares the standard coupler kick (similar to that used in the Mark 0) to that from the Mark 1 racetrack coupler for 100 MV/m peak electric field. The scale for the two couplers differs by a factor of 100. The coupler optimization results were confirmed with the particle tracking code IMPACT-T using 3D electromagnetic field maps generated with the ACE3P codes OMEGA3P and S3P using 3rd order maps for high accuracy. The achievable emittance was lowered from 1 mm mrad to ≈ 0.5 mm mrad [28]. IMPACT-T simulations

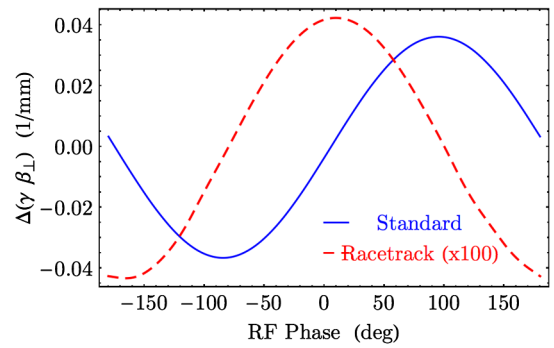


FIG. 6. Comparison of the quadrupole kick versus rf phase for the Mark 1 gun racetrack coupler with that if a standard (round) coupler had been used, normalized to 100 MV/m peak electric field. The scale for the racetrack coupler has been magnified by 100 times

using these 3D maps and then 2D field maps confirm that the influence of residual coupler asymmetry on the bunch emittance is negligible.

D. Final 3D design

The full 3D rf design for the rf gun was accomplished using HFSS. Each modification to the design has a different sensitivity: the field flatness is primarily a function of relative cell radii; the coupling is primarily a function of the coupler cell radius and coupling aperture; and the frequency is primarily changed by scaling all cell radii. However, when trying to fix one of these parameters, the other two also change to some extent. The final design was achieved by successive iteration, until all parameters were simultaneously met: a π -mode frequency of 11.424 GHz, a $<1\%$ field flatness, and a coupling β of ~ 1.7 .

Final modification of the design was necessary to converge on a set of dimensions for engineering drawings and fabrication. Machining will be done at 20°C , while operation is planned for 45°C . The design dimensions were thus scaled for the temperature difference and then truncated to acceptable fabrication tolerances. Final dimensional adjustments were then made to ensure the desired parameters would be achieved at 45°C .

Final design results were used for various beam dynamics modeling. In some cases, e.g., in PARMELA and ASTRA runs, these were 2D axially symmetric design results which

most closely matched the final design, in others, e.g., in ACE3P and IMPACT-T, the full 3D geometry was used to accurately gauge the impact of wakefields or coupler asymmetry.

III. BEAM DYNAMICS

Beam dynamics modeling was done as well to optimize the overall photoinjector design, in particular, by adjusting the bunch phase, solenoid strength, and the gun-to-accelerator-structure spacing to achieve the best emittance compensation. Initial modeling determined the emittance achievable in the photoinjector, and set the scale for errors that were acceptable in magnet misalignments, multipole field components, etc.

A serendipitous result of the collaboration on this photoinjector design was that multiple beam dynamics codes were brought to bear on the problem, and the results were able to be checked across codes. Because the physics included in many of these codes was not entirely overlapping, single sources of emittance growth were identifiable.

A. Photoinjector performance

Figure 7 shows PARMELA results on the normalized rms emittance and rms size of a 250 pC bunch as a function of distance along the photoinjector. A thermal emittance of 0.9 mm mrad per mm rms of laser spot size was assumed

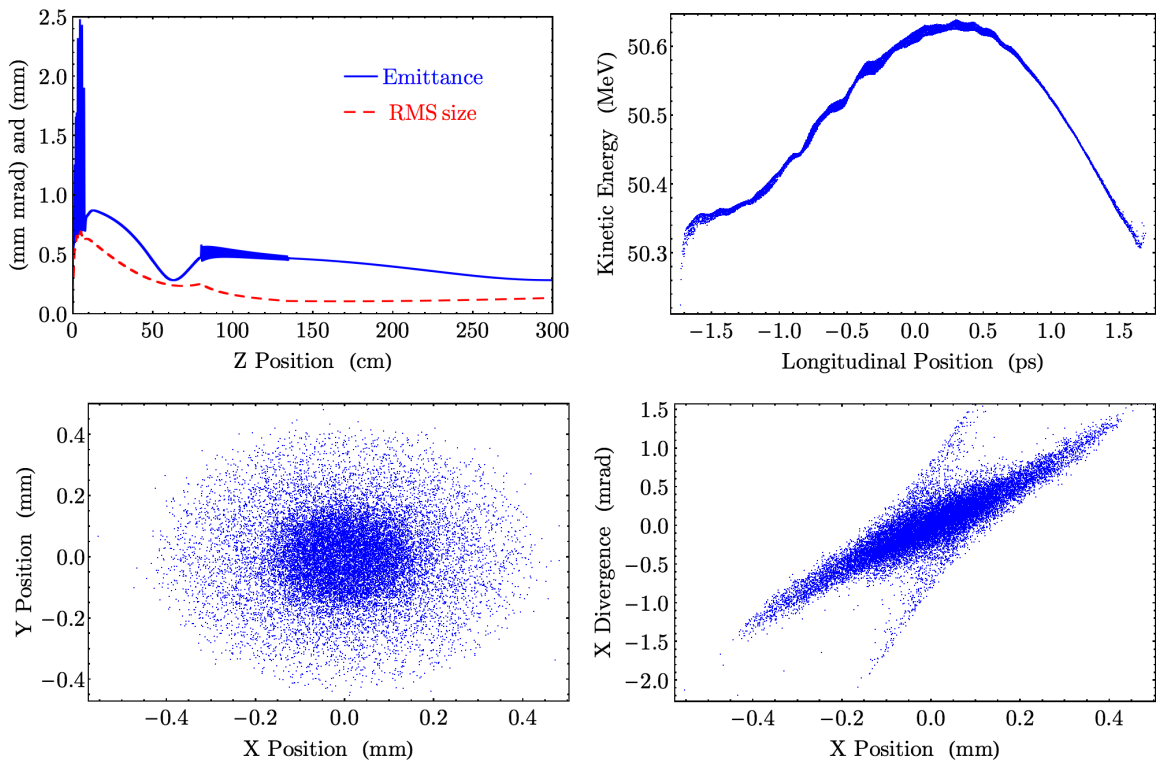


FIG. 7. PARMELA simulation X position (mm) results for the Mark I X-band rf gun and a single T53 accelerator section: normalized transverse emittance and beam size; kinetic energy gain through the length of the rf gun; kinetic energy as a function of longitudinal position within the bunch; x phase space of macroparticles.

following [30]. The energy gain of the electron bunch in the Mark 1 rf gun is also shown in Fig. 7, along with the energy distribution within the bunch, and the x phase space. An emittance of 0.35 mm mrad and an energy spread of 0.2% are expected at 50 MeV for a 250 pC bunch, which requires the use of the Mark 1 rf gun and a single T53 accelerator structure operating at 75 MV/m. The T53 is a $2\pi/3$ phase advance per cell traveling, constant gradient structure [31] which is modeled in PARMELA using the appropriate *trwave* commands and POISSON input. The emittance at the end of the 250 MeV VELOCIRAPTOR linac is expected to be 0.35 mm mrad for a 250 pC bunch [9], which includes the Mark 1 rf gun and six T53 accelerator structures operating at 75 MV/m. ASTRA and IMPACT-T results confirm the PARMELA predictions for beam quality using 3D rf field maps.

B. Lower gradient operation

The Mark 0 rf gun was operated at 200 MV/m, but achieving this high of gradient is a concern [11,12]. To mitigate possible high dark current issues, and with a view to run with higher repetition rates, operation at lower peak surface fields was investigated. Beam dynamics modeling was repeated at lower peak fields, and the emittance compensation optimization was repeated in each case. Very good emittances and relatively small bunches could still be obtained at lower peak fields.

Once emittance compensation is reoptimized, the direct effect of lower gradient operation was seen. Operation at a reduced peak surface electric field of 180 MV/m produced a $\approx 10\%$ increase in emittance, and operation at 140–160 MV/m produced a $\approx 50\%$ increase in emittance. Sustained operation at a lower peak field would motivate a complete redesign of the photoinjector, and would prompt some reconsiderations as to optimal design decisions;

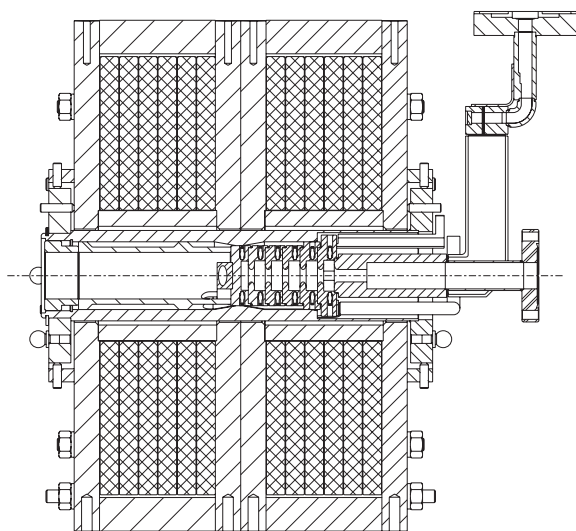


FIG. 8. Schematic of the emittance compensation solenoid fitted with the Mark 1 rf gun and precision alignment sleeve.

lower gradient operation is considered here only as a risk mitigation due to surface preparation effects or damage. At lower gradients, the first cell length optimum is shorter: for 100 MV/m peak electric field, a 5.4 cell rf gun would perform better than the 5.59 cell gun [32].

C. Emittance compensation solenoid

A 6 kG emittance compensation solenoid similar to that used with the Mark 0 rf gun has been fabricated, featuring full insertion of the rf gun within the solenoid. The magnet consists of two identical halves, which serve to cancel the field in the center, where the rf gun cathode is positioned. Each half is made up of six pancake coils aligned with their current feeds alternating left and right for minimal field disturbance. Each pancake coil is made of square cross-section copper wire, with a circular water-cooling channel, wound into two spiraling layers, the first spiraling in, and the second spiraling out. The arrangement of the coils can be seen in Fig. 8.

Magnet misalignments both steer and focus the electron beam outside its design trajectory, which can increase the bunch emittance due to dispersion and nonlinear rf field effects. PARMELA results for transverse solenoid offsets are shown in Fig. 9; this predicted level of emittance growth has been used to set tolerances for solenoid alignment. This solenoid will be aligned through precision engineering of the rf gun mounting parts, which is discussed in more detail in Sec. IV B.

The emittance compensation solenoid has been fabricated at SLAC. The magnetic field multipole components have been measured experimentally by SLAC metrology using a rotating coil technique: a 2.54 cm length coil is rotated at a radial distance of 2.714 cm, and a Fourier analysis of the induced signals yields multipole moments. Results are shown in Fig. 10 for the dipole, quadrupole, sextupole, and octupole moments at the maximum 300 A current, which corresponds to a peak solenoid field of 7122 G. The multipole moments were converted into full

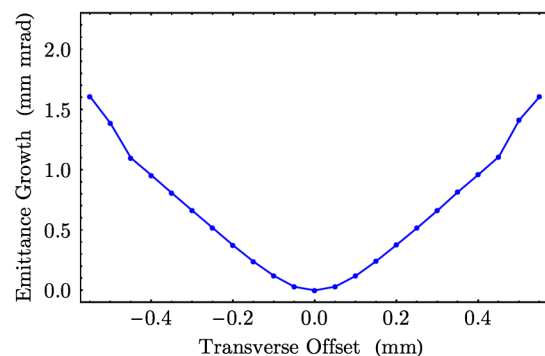


FIG. 9. Normalized bunch emittance growth calculated by PARMELA as a function of transverse offset of the solenoid. The photoinjector and bunch parameters are the same as those discussed for Fig. 7.

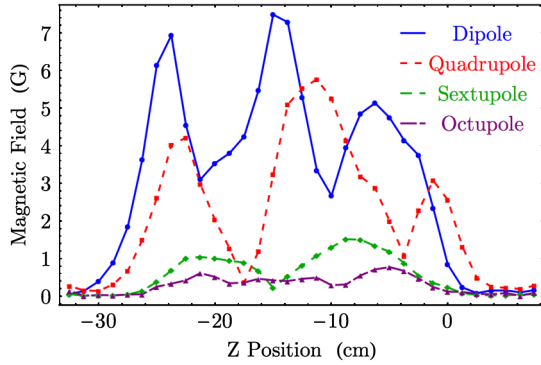


FIG. 10. Multipole magnetic field measurements of the emittance compensation solenoid at the maximum current of 300 A.

3D field maps by using each longitudinal data point at a fixed radius to scale a corresponding 3D multipole field. A linear interpolation was used between data points, and beam dynamics modeling was completed using IMPACT-T with full 3D field maps of the rf gun. Addition of the scaled multipole moments produced $\leq 10\%$ emittance growth. Field correction coils are under consideration to reduce this source of emittance growth.

D. Beam offset

Laser pointing and centering errors can result in a non-centered electron beam, which will then oscillate as it travels through the rf gun. A laser alignment of $<100 \mu\text{m}$ has been specified, and achieved in a similar system [5]. The result of this level of beam offset has been modeled and results in $<0.1 \text{ mm mrad}$ emittance growth, and $\leq 100 \mu\text{m}$ of beam offset, which can be corrected with magnetic steering coils. ACE3P simulations with a full wakefield calculation are consistent with these results. On-axis injection into the T53 accelerator section will be maintained using two sets of x - y steering coils as necessary.

E. Mode beating

Using the full 3D fields of the X-band rf gun, beam dynamics simulations were done to model the effects of all

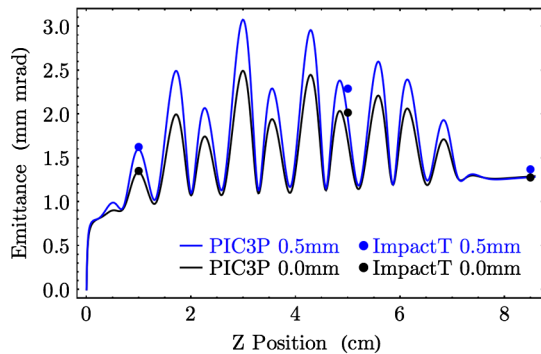


FIG. 11. Evolution of the transverse emittance along the X-band gun simulated with PIC3P and comparison with IMPACT-T at 3 sampled longitudinal points.

modes excited in the gun as modeled in II B. In steady state, after several rf gun fill times, the highest level of other excited modes is the nearest neighboring mode (which is 25 MHz lower in frequency with a β of ~ 3), at a level of $\leq 2\%$ (due to the rf losses in the cavity, not just the π mode is excited in steady state). The emittance impact of this and all other modes in steady state was seen to be less than 1%. During the transient filling of the gun, much higher levels of other modes can be excited, though by 160 ns of filling, a level of $\leq 2\%$ is reached.

F. Wakefields

Fully self-consistent wake calculations have begun using the PIC code PIC3P from the ACE3P suite [19,20]. ACE3P results confirm the beam offset specification is sufficient, and that wakefields in the photoinjector will not significantly impact single bunch 250 pC operation. Future simulations will take advantage of the full computational ability of the ACE3P suite of codes, but the results of this initial series of runs form a basis for this work going forward. For the bulk of the modeling effort on the Mark 1 rf gun, the simplest code that is sufficient was used, with more complex codes used for cross-benchmarking.

A fully 3D program, IMPACT-T, was also used to track particles taking into account space charge forces, and the 3D rf fields in the structures, including the quadrupole component of the couplers [33]. The effect of misalignments of the various elements, including the drive-laser, rf gun, solenoid, and accelerator structures, were evaluated.

ACE3P simulation results show good general agreement with IMPACT-T results, as shown in Fig. 11. Simulations were done for an on-axis initial electron bunch and for a bunch with an initial 0.5 mm offset. Minor differences toward the end of the rf gun are suspected to stem from the differing treatment of boundary conditions.

IV. TESTING PLANS

A. Beam line symmetry

In order to maintain the electron beam brightness, considerable effort was taken to fully symmetrize the photoinjector beam line, especially before the 7 MeV electrons arrive at the accelerator section. The low energy beam line is visible in the CAD rendering in Fig. 12. The rf gun itself has been symmetrized as discussed in Sec. II C. Vacuum pumping on the beam line is done through a wrap-around symmetric feed, so that the beam sees primarily the round pipe, with small holes providing vacuum conductance and much smaller asymmetry than a simple T-junction. A vacuum valve is used to provide isolation of the gun, and an rf version has been procured that provides a smooth and symmetric aperture when the valve is open. A specially designed pneumatically operated pop-in screen has been fabricated so that when the screen is withdrawn a smooth beam pipe is seen by the electron beam, as shown in Fig. 13. Finally, the laser mirror has been placed external

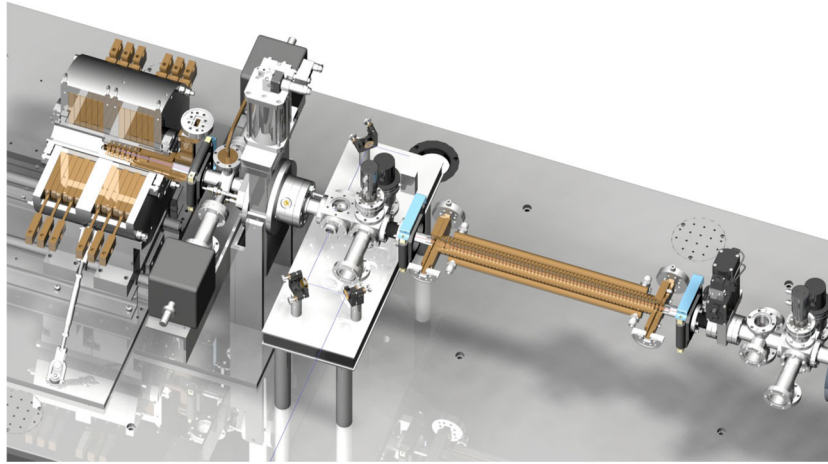


FIG. 12. CAD rendering of the X-band rf photoinjector: Mark 1 rf gun, emittance compensation solenoid, low energy beam line, and T53 accelerator section.

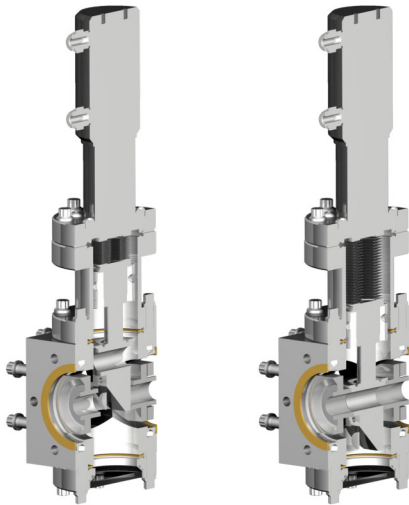


FIG. 13. CAD rendering of a pop-in screen showing symmetrized insertion of the vacuum pipe when the screen is withdrawn.

to a smaller aperture beam pipe so that the electron beam does not see the asymmetry of two 45° UV mirrors, but a smooth beam pipe.

B. Fabrication

Engineering drawings have been completed using the electromagnetic design dimensions, and the closed loop cross-checking discussed in Sec. II D. Dimensions are called out to $2.5 \mu\text{m}$ accuracy on critical parts such as the cell diameters, and toleranced to $\pm 5 \mu\text{m}$. Tuning is capable of producing $\sim 5 \text{ MHz}$ frequency shifts per cell, which corresponds to a $\sim 5 \mu\text{m}$ fabrication error; four push/pull tuning pins are included in each cell, and can be effectively used more than once; if necessary an additional round of tuning can be done by reannealing the structure. To significantly change the coupling β requires

retuning all of the gun cells, which was part of the motivation of choosing a design β in the middle of the optimal range. The frequency can be tuned by changing the operating temperature, which shifts the resonant frequency by $190 \text{ kHz}/^\circ\text{C}$. Because the cells will be diffusion bonded, mating surfaces will be diamond turned to $2 \mu\text{m}$ flatness. The high temperature (1040°C) diffusion bonding cycle will also leave a very clean copper surface with large regrown grains, perfect for high gradient operation.

At LLNL, an alignment socket will be used to fix the rf gun position relative to the magnetic center of the emittance compensation solenoid and the rest of the test station hardware. The precision sleeve is shown in Fig. 8 and is capable of meeting alignment tolerances of $\pm 125 \mu\text{m}$ both transversely and longitudinally. The alignment socket also provides for thermal ballast against temperature variation across the gun surface, or deviations from the operating temperature due to air currents or thermal fluctuations in the room.

C. Mark 2 design

There are many possible improvements that have been identified during the Mark 1 design process that will be considered for inclusion in a Mark 2 rf gun design.

Achieving low emittance requires laser injection at the correct phase, which will require $\lesssim 1^\circ$ phase accuracy and stability. Field probes in the gun itself would enable a direct measurement, but were deemed a complicated addition given the operation at high peak fields, and the space constraints in an X-band structure. Several probe geometries are undergoing preliminary design currently, and may be included in the next generation of X-band rf gun. The phase measurement plan for the Mark 1 photoinjector will rely on the reflected power measured from the directional coupler on the gun rf feed. As discussed in Sec. II B, the sensitivity of $\gtrsim 5^\circ/^\circ\text{C}$ has been deemed sufficient for diagnostics purposes.

The high current carrying technology used in the emittance compensation solenoid leads to tight tolerances on the current leads and coil crossovers. As noted in Sec. III C, dipole errors on the order of 5 G have been measured when the solenoid is operated at its full field strength of 6 kG. Correction of field errors may be necessary with secondary or even tertiary coils, which will be accomplished with thin corrector coils around the alignment socket. In the future, a move to an alternate magnet technology is being considered in which more turns of lower current wire are used so that the error induced by connections and crossovers is reduced.

The Mark 1 rf gun uses the same single channel cooling geometry used in the Mark 0 gun. The single channel provides both heating of the gun to its 45° operating temperature and removal of excess heat from Ohmic losses in the copper. Because a single channel is used, there is some small dipole asymmetry, which has been calculated and predicted to have a negligible effect. Sensitivity to thermal asymmetry will however increase as the gun is operated at higher gradients, higher instantaneous pulsed heating temperature rises, and increasing repetition rates. A quadrupole symmetric geometry or even a cylindrically symmetric jacket are under consideration for the Mark 2 design if it appears necessary during testing of the Mark 1 rf gun.

A fixed photocathode surface is clearly both a lifetime and risk liability, and the move to a removable photocathode is the highest priority for inclusion in the Mark 2 design. A removable photocathode would extend the lifetime of the remaining gun structure, decrease downtime between cathode/gun replacement, and enable photocathode material research and advancements.

D. Testing facilities

Two copies of the Mark 1 rf gun are being built for testing at LLNL and SLAC. Testing at LLNL will take place at the X-band Test Facility; testing at SLAC will take place at the X-band Test Accelerator (XTA) at the NLCTA.

E. LLNL testing

The advanced X-band test station will be an independent beam line capable of performing experiments on future improvements to the LLNL Nuclear Photonics Facility. Until the full facility is built in B391, the test station will be established in the shielded caves of B194. Early establishment of the test station will enable operational experience and allow multibunch experiments to begin in advance of the full B391 facility being available for occupancy. The parameters for the test station are shown in Table IV. The test station will consist of a control room with equipment racks, a high power solid-state modulator and XL-4 klystron, rf distribution waveguide, a Mark 1 rf gun, and a single traveling wave accelerator section with beam line transport magnets and diagnostics. The system is discussed in more detail elsewhere: the beam dynamics in

TABLE IV. LLNL test station parameters.

Charge	250 pC
Bunch duration	2 ps
Bunch rise/fall	<250 fs
Normalized emittance	≲ 0.5 mm mrad
Gun energy	7 MeV
Cathode field	200 MV/m
Coupling β	1.7
Section gradient	~75 MV/m
Final energy	30–50 MeV

[34], laser systems in [22], rf distribution system in [35], and complete test station [36].

F. SLAC testing

The XTA X-band photoinjector at the SLAC NLCTA has the potential of producing bunch emittances that are comparable or better than those at the LCLS injector, but with a 3 times shorter bunch length, which would make subsequent bunch compression simpler [32]. The beam line includes a 105 cm long X-band acceleration section (T105) which takes the electron beam up to 100 MeV and an electron beam measurement station. Other X-band photoinjectors such as the UCLA hybrid gun [37] will be characterized at this facility.

The XTA beam line will be installed in a 6.7 m region at the downstream end of the NLCTA tunnel. The gun, gun-to-linac section, and T105 accelerator will use 1.7 m leaving 5 m for beam characterization. More detail is available in conference proceedings, including [32].

V. CONCLUSION

The design for a next generation X-band rf gun (the Mark 1) was presented. It will be tested at new beam lines being constructed at LLNL and SLAC that include X-band accelerators. With 250 pC bunches, emittances of ≲ 0.5 mm mrad are expected. Such rf photoinjectors would be ideal for compact x-ray free-electron lasers and Compton photon sources, such as the plan to produce monoenergetic gamma rays at LLNL.

ACKNOWLEDGMENTS

The authors would like to thank the LLNL design review committee members: Bernie Merritt, Dennis Atkinson, Ken Kasper, Juan Barraza, Carl Ekdahl, Jamie Rosenzweig, and Sami Tantawi. The authors would also like to thank Jake Haimson and Dave Dowell for useful comments and suggestions. This work was performed under the auspices of the U.S. Department of Energy by Lawrence Livermore National Laboratory under Contract No. DE-AC52-07NA27344; this work also supported by the U.S. Department of Energy under Contract No. DE-AC03-76SF00515.

- [1] F. V. Hartemann, W. J. Brown, D. J. Gibson, S. G. Anderson, A. M. Tremaine, P. T. Springer, A. J. Wootton, E. P. Hartouni, and C. P. J. Barty, *Phys. Rev. ST Accel. Beams* **8**, 100702 (2005).
- [2] J. Pruet, D. P. McNabb, C. A. Hagmann, F. V. Hartemann, and C. P. J. Barty, *J. Appl. Phys.* **99**, 123102 (2006).
- [3] F. V. Hartemann, F. Albert, C. W. Siders, and C. P. J. Barty, *Phys. Rev. Lett.* **105**, 130801 (2010).
- [4] F. Albert, S. G. Anderson, G. A. Anderson, S. M. Betts, D. J. Gibson, C. A. Hagmann, J. Hall, M. S. Johnson, M. J. Messerly, V. A. Semenov, M. Y. Shverdin, A. M. Tremaine, F. V. Hartemann, C. W. Siders, D. P. McNabb, and C. P. J. Barty, *Opt. Lett.* **35**, 354 (2010).
- [5] D. J. Gibson, F. Albert, S. G. Anderson, S. M. Betts, M. J. Messerly, H. H. Phan, V. A. Semenov, M. Y. Shverdin, A. M. Tremaine, F. V. Hartemann, C. W. Siders, D. P. McNabb, and C. P. J. Barty, *Phys. Rev. ST Accel. Beams* **13**, 070703 (2010).
- [6] F. Albert, S. G. Anderson, D. J. Gibson, C. A. Hagmann, M. S. Johnson, M. Messerly, V. Semenov, M. Y. Shverdin, B. Rusnak, A. M. Tremaine, F. V. Hartemann, C. W. Siders, D. P. McNabb, and C. P. J. Barty, *Phys. Rev. ST Accel. Beams* **13**, 070704 (2010).
- [7] F. Albert, S. G. Anderson, D. J. Gibson, R. A. Marsh, S. S. Wu, C. W. Siders, C. P. J. Barty, and F. V. Hartemann, *Phys. Rev. ST Accel. Beams* **14**, 050703 (2011).
- [8] F. Albert, S. G. Anderson, D. J. Gibson, R. A. Marsh, C. W. Siders, C. P. J. Barty, and F. V. Hartemann, *Phys. Plasmas* **18**, 013108 (2011).
- [9] S. G. Anderson, F. Albert, A. J. Bayramian, G. Beer, R. E. Bonanno, R. R. Cross, G. Deis, C. A. Ebberts, D. J. Gibson, F. V. Hartemann, T. L. Houck, R. A. Marsh, D. P. McNabb, M. J. Messerly, R. D. Scarpetti, M. Y. Shverdin, C. W. Siders, S. S. Wu, C. P. J. Barty, C. E. Adolphsen, T. S. Chu, E. N. Jongewaard, Z. Li, C. Limborg, S. G. Tantawi, A. E. Vlieks, F. Wang, J. W. Wang, F. Zhou, and T. O. Raubenheimer, *Nucl. Instrum. Methods Phys. Res., Sect. A* **657**, 140 (2011).
- [10] C. Limborg, S. Gierman, and J. Power, in *Proceedings of the 20th Particle Accelerator Conference, Portland, OR, 2003* (IEEE, New York, 2003), pp. 2667–2669.
- [11] A. E. Vlieks, G. Caryotakis, W. R. Fowkes, E. N. Jongewaard, E. C. Landahl, R. Loewen, and N. C. Luhmann, Jr., *AIP Conf. Proc.* **625**, 107 (2002).
- [12] A. E. Vlieks, G. Caryotakis, C. DeStefano, J. P. Heritage, E. Landahl, N. C. Luhmann, Jr., D. Martin, and A. Menegat, *AIP Conf. Proc.* **691**, 358 (2003).
- [13] A. E. Vlieks, R. Akre, G. Caryotakis, C. DeStefano, W. J. Frederick, J. P. Heritage, N. C. Luhmann Jr., D. Martin, and C. Pellegrini, *AIP Conf. Proc.* **807**, 481 (2006).
- [14] L. Young and J. Billen, in *Proceedings of the 20th Particle Accelerator Conference, Portland, OR, 2003* (Ref. [10]), pp. 3521–3523.
- [15] Los Alamos Accelerator Code Group [<http://laacg1.lanl.gov/>].
- [16] ANSYS HFSS [<http://www.ansys.com/>].
- [17] J. Qaing, LBNL Paper No. LBNL-62326, 2010 [<http://www.escholarship.org/uc/item/2sw7g9c3>].
- [18] K. Floettmann, ASTRA [http://www.desy.de/~mpyfl/Astra_dokumentation/].
- [19] Z. Li, V. Akcelik, A. Candel, S. Chen, L. Ge, A. Kabel, L.-Q. Lee, C. Ng, E. Prudencio, G. Schussman, R. Uplenchwar, L. Xiao, and K. Ko, in *Proceedings of the 16th IEEE International Pulsed Power Conference, Albuquerque, NM* (IEEE, Piscataway, NJ, 2007), pp. 889–893.
- [20] K. Ko, A. Candel, L. Ge, A. Kabel, R. Lee, Z. Li, C. Ng, V. Rawat, G. Schussman, and L. Xiao, in *Proceedings of the 2010 Linear Accelerator Workshop* (Tsukuba, Japan, 2010), pp. 1028–1032.
- [21] O. Nezhvenko, D. Myakishev, V. Tarnetsky, and V. Yakovlev, in *Proceedings of the 1995 Particle Accelerator Conference, Dallas, TX* (IEEE, New York, 1996), pp. 1076–1078.
- [22] D. J. Gibson, F. Albert, C. P. J. Barty, A. J. Bayramian, C. A. Ebberts, F. V. Hartemann, R. A. Marsh, and M. J. Messerly, in *Proceedings of the 2011 Particle Accelerator Conference* (IEEE, New York, 2011), pp. 2540–2542.
- [23] D. P. Pritzkau and R. H. Siemann, *Phys. Rev. ST Accel. Beams* **5**, 112002 (2002).
- [24] S. V. Kuzikov and M. E. Plotkin, *Radiophys. Quantum Electron.* **50**, 885 (2007).
- [25] F. Wang, C. Adolphsen, and C. Nantista, *Phys. Rev. ST Accel. Beams* **14**, 010401 (2011).
- [26] F. Wang, C. Adolphsen, and C. Nantista, in *Proceedings of the 2011 Particle Accelerator Conference* (Ref. [22]), pp. 1094–1096.
- [27] Z. Li, J. Chan, L. D. Bentson, D. H. Dowell, C. Limborg-Deprey, J. F. Schmerge, D. Schultz, and L. Xiao, in *Proceedings of the 21st Particle Accelerator Conference, Knoxville, 2005* (IEEE, Piscataway, NJ, 2005), pp. 2176–2178.
- [28] Z. Li, F. Zhou, A. Vlieks, and C. Adolphsen, in *Proceedings of the 2011 Particle Accelerator Conference* (Ref. [22]), pp. 2044–2046.
- [29] W. K. H. Panofsky and W. A. Wenzel, *Rev. Sci. Instrum.* **27**, 967 (1956).
- [30] D. H. Dowell and J. F. Schmerge, *Phys. Rev. ST Accel. Beams* **12**, 074201 (2009).
- [31] C. Adolphsen *et al.*, in *Proceedings of the 20th Particle Accelerator Conference, Portland, OR, 2003* (Ref. [10]), pp. 668–672.
- [32] C. G. Limborg-Deprey, C. Adolphsen, S. Chu, M. Dunning, K. Jobe, E. Jongewaard, C. Hast, A. E. Vlieks, F. Wang, D. Walz, R. A. Marsh, S. G. Anderson, F. V. Hartemann, and T. Houck, in *Proceedings of the 2011 Particle Accelerator Conference* (Ref. [22]), pp. 133–135.
- [33] F. Zhou, C. Adolphsen, Y. Ding, Z. Li, and A. Vlieks, F. Zhou *et al.*, in *Proceedings of the 2010 International Particle Accelerator Conference, Kyoto, Japan* (ICR, Kyoto, 2010), pp. 1761–1763.
- [34] S. G. Anderson, F. Albert, C. P. J. Barty, G. Deis, C. A. Ebberts, D. J. Gibson, F. V. Hartemann, T. L. Houck, R. A. Marsh, C. Adolphsen, A. Candel, E. N. Jongewaard, Z. Li, C. Limborg-Deprey, T. Raubenheimer, S. G. Tantawi, A. E. Vlieks, F. Wang, J. W. Wang, and F. Zhou, in *Proceedings of the 2011 Particle Accelerator Conference* (Ref. [22]), pp. 334–336.
- [35] R. A. Marsh, S. G. Anderson, G. K. Beer, R. R. Cross, G. A. Deis, C. A. Ebberts, D. J. Gibson, F. V. Hartemann, T. L. Houck, C. P. J. Barty, C. Adolphsen, A. Candel, T. S.

- Chu, E. N. Jongewaard, Z. Li, S. G. Tantawi, A. Vlieks, F. Wang, J. W. Wang, F. Zhou, and T. Raubenheimer, in Proceedings of the 2011 Particle Accelerator Conference (Ref. [22]), pp. 1082–1084.
- [36] R. A. Marsh, F. Albert, S. G. Anderson, G. Beer, R. R. Cross, G. A. Deis, C. A. Ebberts, D. J. Gibson, F. V. Hartemann, T. L. Houck, C. P. J. Barty, C. Adolphsen, A. Candel, T. S. Chu, E. N. Jongewaard, Z. Li, C. Limborg-Deprey, S. G. Tantawi, A. E. Vlieks, F. Wang, J. W. Wang, F. Zhou, T. O. Raubenheimer, in Proceedings of the 2011 Particle Accelerator Conference (Ref. [22]), pp. 235–237.
- [37] B. Spataro, A. Valloni, D. Alesini, N. Biancacci, L. Faillace, L. Ficcadenti, A. Fukusawa, L. Lancia, M. Migliorati, F. Morelli, A. Mostacci, B. O’Shea, L. Palumbo, J. B. Rosenzweig, A. Yakub, *Nucl. Instrum. Methods Phys. Res., Sect. A*, **657**, 99 (2011).